Optics Letters

Ultrasensitive optofluidic resonator refractive index sensor

Zhiyuan Xiao, Hailang Dai, and Xianfeng Chen*

The State Key Laboratory on Fiber Optic Local Area Communication Networks and Advanced Optical Communication Systems, School of Physics and Astronomy, Shanghai Jiao Tong University, Shanghai 200240, China
**Corresponding author: xfchen@sjtu.edu.cn*

Received 4 July 2018; revised 1 August 2018; accepted 2 August 2018; posted 2 August 2018 (Doc. ID 337766); published 27 August 2018

We report an optofluidic resonator refractive index sensor based on an integrated structure constructed by a free-space coupling architecture. It uses a symmetrical metal-cladding hollow-core waveguide and a prism to generate surface plasmon polarization. The sensor achieves very high sensitivity by coupling the core mode to ultrahigh-order modes in the waveguide layer that can obtain a refractive index of a detailed low-order value of 1×10^{-6}. We demonstrate the device through infiltration of different fluids into the hollow core along an optofluidic resonator. A detection limit of 1.0×10^{-6} refractive index units has been derived from measurements. The presented method can be applied to the detection of molecular structures and biochemistry.

OCIS codes: (280.0280) Remote sensing and sensors; (280.4788) Optical sensing and sensors; (230.0230) Optical devices; (230.7370) Waveguides.

https://doi.org/10.1364/OL.43.004216

High-precision measurement of the refractive index (RI) is very important and popular in the fields of sensors, medicine, biology, and molecular structure [1]. In the context of detection of biomolecules, the optical detection of small changes in the RI within solutions has received considerable attention recently. In optical detection technology, label-free detection does not require the sample, usually a liquid analyte, to be marked with fluorescent dyes but rather relies on the detection of tiny RI changes due to bonding events, e.g., antibody–antigen interaction. The ability to detect smaller concentrations of molecules results from the smaller detection limits of changes in the RI. Actually, there are a number of optical platforms designed to achieve lower limits of changes of the RI, and their schemes have been investigated with the aim of realizing simple, highly sensitive, real-time optical biosensors capable of working with small analyte volumes [2]. Due to reduced analyte volumes, the integration of analyte waveguide channels in optical structures provides a means to enhance the performance of resonant RI sensors, increase sample-mode interaction and thus to enhance sensitivity [3]. Many fiber-based surface plasmon resonance (SPR) sensors have been reported. So far, different SPR sensor configurations with multimode, single-mode, and polarization maintaining fibers coated with a thin metallic layer have been proposed [4–6], for instance, high-quality microfluidic channel photonic crystal fibers (PCFs) [7], which can be controllably filled with ultra-small volumes of analytes (femtoliter to subnanoliter). Owing to their proximity to the optical core, these channels can have good overlap with the optical mode of the fiber, making them a natural candidate for sensing schemes. Existing PCF RI sensors rely on the shift in wavelength of a resonant feature, which may be introduced by interferometric arrangements, a Bragg or long period grating (LPG) [8], or by bandgap effects [9]. To date, the most sensitive PCF sensors demonstrated rely on a long period fiber grating in a fluid-filled PCF with a maximum sensitivity of 1500 nm/RI unit (RIU) and a detection limit of 1.0×10^{-5} RIU [10]. The evanescent waves in PCFs allow the excitation of the surface plasmon waves supported by a thin metallic layer that coats the fiber. Optical fibers, and also miniature optical spectrum analyzers, allow the development of low-cost, very compact, and portable SPR sensors that can be used for the detection of different analytes in the field. However, the resonant features of evanescent waves are generally broad, limiting the achievable detection limit [11]. Recently, some original resonators have enriched the RI sensor field, such as microring resonator [12–14] and silicon microring resonator [15]. L. Gounaridis achieved a high-performance RI sensor based on low Q-factor ring resonators and fast Fourier transform (FFT) processing of wavelength scanning data and extended the detection limit to approximately 8.5×10^{-7} RIU [14].

Here, we describe a sensor architecture that integrates a hollow-core metal-cladding optofluidic resonator and a prism to generate surface plasmon polarization. Our strategy can be described as follows. A series of discrete guided modes can be excited at certain extremely small incident angles (incident angle $\theta_i < 5°$). These modes are called ultrahigh-order modes (UOMs) [16] in our terminology, since the order of these modes is extremely large, and their effective RI is small when the incident angle fulfills the phase match condition [17]. However, the light beam is coupled from free space with a large incident angle. It is difficult to differentiate the adjacent guide modes because the mode density in the optofluidic resonator is extremely large, and the corresponding attenuated

total reflection (ATR) dips overlap with each other. Meanwhile, when the incident angle reaches the SPR resonance angle (incident angle $\theta_i > 30°$), the surface plasmon polariton (SPP) is excited due to evanescent field oscillation. In the study, the RI of the analyte in the optofluidic resonator undergoes a change of 1.0×10^{-6} RIU, which results in the UOMs shift of approximately 0.014°. Referring to the existed research [18–21], we define the sensitivity of our sensor as the shift of UOM dip per unit variation of the RI. This means a sensitivity of 700°/RIU for transverse electric (TE) and transverse magnetic (TM) modes [22]. For comparison, in the symmetrical waveguide sensor presented [18], the experimentally achieved SPP-mode sensitivity of the TM mode is 1.0×10^{-2} RIU (33.5°/RIU). The figure of merit (FOM) can be defined as FOM $= \Delta T/(T \cdot \Delta n)$, where T denotes reflectance, and Δn denotes RI variation [19]. At the UOM dip, FOM is calculated to be 9×10^5. This research combines the SPR technology and the UOMs and successfully creates a new chip, which combines the symmetrical metal-cladding hollow-core waveguide (SMHW) and the prism, as shown in Fig. 1. It can scan for the angles of SPP and UOMs as a whole structure instead of operating as two separate parts. Measuring the SPP can roughly determine the range of the analyte RI. Then, by using the five continuous UOMs, measurement of the exact value of the RI can be achieved.

As shown in Fig. 1(a), the optofluidic resonator consists of five layers from top to bottom. The middle three layers form the guiding layer to support oscillating guided modes. From the top to bottom, these five layers are a 40 nm Ag coupling layer, a 0.1 mm sample layer, another 0.3 mm high glass cylinder, and a 300 nm Ag substrate. The size of the circle sample channel is 0.12 mm $\times \pi \times$ 0.1 mm^2. All parts are optically contacted with excellent parallelism, except the Ag layers are prepared by thermal evaporation coating technology. A 40 nm Ag film has been constructed at the bottom of the prism, which plays two different roles in chips. On one hand, it is used to excite the SPP combination with the prism, as shown in Fig. 1(b). On the other hand, it acts as a coupling layer for SMHW, as seen in Fig. 1(c). When the light beam is coupled from free space with a large incident angle, it is difficult to differentiate the adjacent guide modes because the mode density in the SMHW is extremely large, and the corresponding ATR dips overlap with each other. Furthermore, a series of discrete guided modes can be excited at certain extremely small incident angles. In our terminology, the orders of these modes are extremely large, and their effective RI is small. From the ray-optical perspective within the same longitudinal propagation distance, the UOM is rebounded at the interfaces more times, and the ray propagation length is longer, since the incident angles of the UOM at the top and bottom interfaces of the guiding layer are extremely small. As a result, the UOMs hold many peculiar optical properties different from the low-order modes.

The numerical simulation demonstrates the resonance modes with varied incident angle conditions, and the curves of resonance modes are plotted. The dielectric constant of the glass and the Ag are $n_1 = 1.51$, $\varepsilon_1 = -18.23 + i0.42$, and $n_2 = 1.0$, respectively. A collimated light beam from a diode laser of 632.8 nm is incident on the top surface of the gold film, and the angular scan is carried out. According to the theory of resonance modes, using boundary conditions, the relationship between reflectivity R and incident angle θ_i can be expressed by Eq. (1) [23]:

$$R = \left| \frac{\gamma_{23} + \gamma_{012} e^{-2\alpha d_2}}{1 + \gamma_{23}\gamma_{012} e^{-2\alpha d_2}} \right|^2. \tag{1}$$

γ_{23} and γ_{012} in Eq. (1) are given by

$$\gamma_{23} = -\frac{i\varepsilon_2 k_3 + \varepsilon_3 \alpha}{-i\varepsilon_2 k_3 + \varepsilon_3 \alpha}, \tag{2}$$

$$\gamma_{012} = \frac{\gamma_{12} + \gamma_{01} e^{2ik_1 d_1}}{1 + \gamma_{12}\gamma_{01} e^{2ik_1 d_1}}, \tag{3}$$

where γ_{12} and γ_{01} are

$$\gamma_{12} = \frac{\varepsilon_1 \alpha + i\varepsilon_2 k_1}{\varepsilon_1 \alpha - i\varepsilon_2 k_1}, \tag{4}$$

$$\gamma_{01} = \frac{i\varepsilon_0 k_1 + \varepsilon_1 \alpha}{i\varepsilon_0 k_1 - \varepsilon_1 \alpha}. \tag{5}$$

In Eqs. (1)–(5), ε_j is the relative permittivity ($j = 0, 1, 2, 3$ means the relative permittivity in the bottom BK7 glass prism, Ag layer, air layer, upper Ag layer, and the BK7 glass cylinder), $\alpha = (\beta^2 - k_0^2\varepsilon_0)^{1/2}$ is the attenuation coefficient of both the upper and bottom Ag layer (for the reason that $\varepsilon_0 = \varepsilon_1$), $k_i = (k_0^2\varepsilon_i - \beta^2)^{1/2}$ is the propagation constant, $\beta = k_0 n_1 \sin\theta_i$, d_1 and d_2 are the thickness of the hollow core of the chip and the upper Ag layer. The numerical simulation result of the curve of resonance modes is shown in Fig. 2(a). A series of dips in the reflectivity spectrum due to the resonant transfer of energy into guided modes (TM) can be clearly observed. As shown in Figs. 2(b) and 2(c), the two parts of modes curves have been presented. Five ATR dips fall in 0°–2°, and only one SPP mode

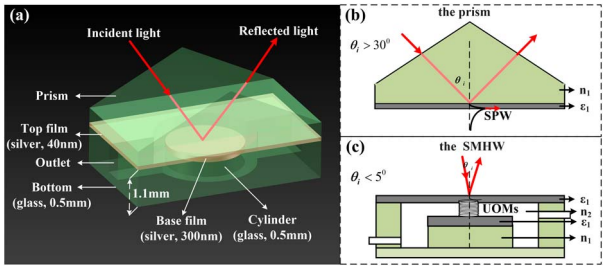

Fig. 1. (a) Optofluidic resonator. (b) The excited SPP composed of Ag film and the prism structure of the optofluidic resonator. (c) The bottom three layers of the optofluidic resonator form a SMHW.

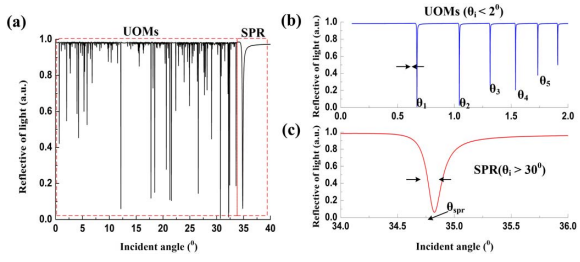

Fig. 2. (a) Numerical stimulation result of the curve of resonance modes. (b) Five ATR dips of UOMs in a range 0°–2°. (c) SPP mode in the range of 34°–36°.

is present in 34°–36°, by which the resonance angle can be obtained.

According to the reflected light function, we need to use global variables to define the following parameters. The RI n_1 of the BK7 prism, the Ag film dielectric constant ε_1 of SMHW, the thickness d_1 of the metal layer in the bottom of the prism, the thickness d_2 of the hollow core, and the incident beam wavelength λ. Meanwhile, we need to define a global variable ε_2 because the dielectric constant of the waveguide layer within the allowable accuracy range needs to be obtained. Defining these variables facilitates us calculating the reflectance curves for different structural coefficients and determining the resonance angle at which the ATR dips appear. In combination with the reflectivity definition in Eq. (1), the R of the SPP can be written with the incident light based on the three-layer waveguide structure. Through calculation, SPP can provide a RI detection limitation of 5.0×10^{-4} RIU. The approximate range of the dielectric constant of the analyte can be calculated in advance using the Matlab program. To obtain highly accurate values of the dielectric constant, we need to redefine the dielectric constant of the waveguide layer when UOMs are excited, which can be set as ε_{20}. This ε_{20} variable with higher accuracy is what we aim to obtain. The minimum division of ε_{20} is the accuracy of the required dielectric constant. ε_{20} falls within the approximate range of the dielectric constant of the analyte determined by SPP, which can be calculated in advance using Matlab. Similarly, the function file $R(\theta i)$ is used to calculate the dip value of the UOMs, which corresponds to each dielectric coefficient indexed in the range of the dielectric coefficient obtained by SPP. With all these values, the exact value of the dielectric coefficient of the analyte can finally be determined. When the accuracy of the angle measurement is reliable, the measured dielectric constant can achieve the RI detection limitation of 1.0×10^{-6} RIU.

The experimental arrangement is presented in Fig. 3. To excite the UOMs of SMHW in small incident angles and SPP at large angles simultaneously, a transverse-excitation-polarized laser beam from a 30 mW, 632.8 nm He–Ne laser (MW-SL-632.8/30 mW, Shanghai Optics Engine Inc. Shanghai, China) with a 0.001 mrad divergence (a 1 mm aperture further reduces the divergence) impinges on the prism bottom. The sample solution is pumped through the cell by an injector with a pipe whose inner radius is 0.5 mm. A computer-controlled $\theta/2\theta$ goniometer performs angular scans, while the intensity of the reflected beam is detected by a photodiode. The ATR dip is recorded for UOMs.

In the experimental data, as shown in Fig. 4, we obtain the UOMs and SPP modes when the analyte has been injected into the hollow core. The RI of the BK7 prism $n_1 = 1.67$, the Ag film dielectric constant $\varepsilon_1 = -18.23 + i0.42$ of SMHW, the

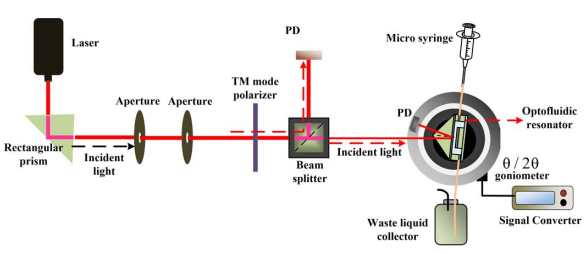

Fig. 3. Experimental system and optofluidic resonator.

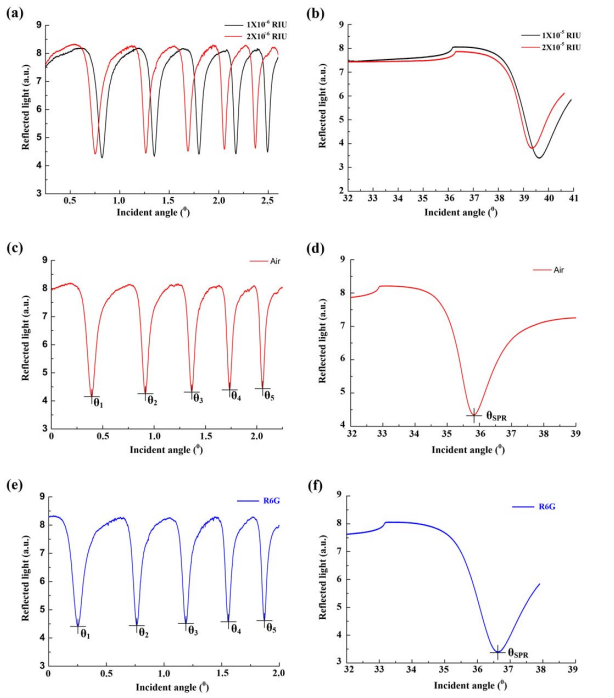

Fig. 4. Experimental data. (a) and (b) UOMs and SPP modes when analytes with different RIs have been injected into the hollow core, respectively. (c) and (d) UOMs and SPP modes when air has been injected into the hollow core, respectively. (e) and (f) UOMs and SPP modes when the 1×10^{-3} mol/L R6G solution has been injected into the hollow core, respectively.

thickness of the metal layer at the bottom of the prism $d_1 = 40$ nm, the thickness $d_2 = 0.1$ mm of the hollow core, and the incident beam wavelength $\lambda = 632.8$ nm. The RI of analyte has been changed by 1×10^{-6} RIU. Correspondingly, modes would shift by approximately 0.014°, but the modes of different RIs can be distinguishable, as shown in Fig. 4(a). However, if the RI of the analyte has been changed by 1×10^{-5} RIU, we discover that the SPP mode would shift too, but the modes of different RIs are intertwined and undistinguishable, as shown in Fig. 4(b). As shown in Figs. 4(c) and 4(d), when air has been injected into the hollow core at a 20°C environment in processing, we can obtain values of θ_1, θ_2, θ_3, θ_4, θ_5, and θ_{SPP} and calculate the RI of air by the Matlab program. In order to verify the accuracy and reliability of the design and Matlab program, we conducted the same experiment with rhodamine 6G (R6G) solution to detect its RI. In Table 1, we present the experiment results of RIs of air and R6G solution. It needs to be noted that the change of temperature will also cause the shift of the ATR dip, but compared to the influence of RI change, this effect is tiny enough for us to ignore.

In summary, this study combines SPR technology and UOMs and successfully creates an optofluidic resonator consisting of an SMHW and prism. This new waveguide can scan for the angles of SPP and UOMs as a whole structure instead of measuring as two parts. Measuring the SPP can roughly figure out the range of the RI and also the thickness of the waveguide. Then, by using the angles of the UOMs, we can figure out the exact value of the RI. By programming with Matlab, this research can automatically calculate the RI of the waveguide.

Table 1. Experiment Result

Samples	Refractive Index by SPR	Refractive Index	Refractive Index by UOMs					Refractive Index
Resonance Angle	θ_{SPR}	n_{SPR}	θ_1	θ_2	θ_3	θ_4	θ_5	n_{UOMs}
Air	35.811	1.0027	0.3211	0.8367	1.3132	1.4864	2.0752	1.002731
Rhodamine 6G	36.625	1.3626	0.2534	0.7584	1.2216	1.5873	1.8037	1.362645

After numerical simulation and experiments, it comes out that the precision of the RI can reach 1.0×10^{-6} RIU as the measurement precision of the angle reaches 1×10^{-4} deg.

Funding. National Key R&D Program of China (2013CBA01703, 2017YFA0303700); National Natural Science Foundation of China (NSFC) (11734011, 61235009).

REFERENCES

1. X. D. Fan, I. M. White, S. I. Shopova, H. Y. Zhu, J. D. Suter, and Y. Z. Sun, Anal. Chim. Acta **620**, 8 (2008).
2. R. A. Potyrailo, S. E. Hobbs, and G. M. Hieftje, Fresenius J. Anal. Chem. **362**, 349 (1998).
3. B. J. Eggleton, C. Kerbage, P. S. Westbrook, R. S. Windeler, and A. Hale, Opt. Express **9**, 698 (2001).
4. L. Rindorf and O. Bang, J. Opt. Soc. Am. B **25**, 310 (2008).
5. N. M. Litchinitser and E. Poliakov, Appl. Phys. B **81**, 347 (2005).
6. L. Rindorf and O. Bang, Opt. Lett. **33**, 563 (2008).
7. I. M. White and X. D. Fan, Opt. Express **16**, 1020 (2008).
8. P. Steinvurzel, E. D. Moore, E. C. Magi, and B. J. Eggleton, Opt. Lett. **31**, 2103 (2006).
9. B. T. Kuhlmey, T. P. White, G. Renversez, D. Maystre, L. C. Botten, C. M. de Sterke, and R. C. McPhedran, J. Opt. Soc. Am. B **19**, 2331 (2002).
10. W. Groh and A. Zimmermann, Macromolecules **24**, 6660 (1991).
11. R. C. Jorgenson and S. S. Yee, Sens. Actuators B **12**, 213 (1993).
12. G. N. Tsigaridas, Photon. Sens. **7**, 217 (2017).
13. G. A. J. Besselink, R. Heideman, E. Schreuder, L. S. Wevers, F. Falke, and H. H. Van den Vlekkert, J. Biosens. Bioelectron. **7**, 209 (2016).
14. L. Gounaridis, P. Groumas, E. Schreuder, G. Tsekenis, A. Maroussis, R. Heideman, H. Avramopoulos, and C. Kouloumentas, Opt. Express **25**, 7483 (2017).
15. W. Bogaerts, P. De Heyn, T. Van Vaerenbergh, K. De Vos, S. Kumar Selvaraja, T. Claes, P. Dumon, P. Bienstman, D. Van Thourhout, and R. Baets, Laser Photon. Rev. **6**, 47 (2012).
16. L. De Maria, M. Martenelli, and G. Vegetti, Sens. Actuators B **12**, 221 (1993).
17. R. Alonso, J. Subías, J. Pelayo, F. Villuendas, and J. Tornos, Appl. Opt. **33**, 5197 (1994).
18. A. Trouillet, C. Ronot-Trioli, C. Veillas, and H. Gagnaire, Pure Appl. Opt. **5**, 227 (1996).
19. J. Chen, Z. Li, Y. Zou, Z. Deng, J. Xiao, and Q. Gong, Plasmonics **8**, 1627 (2013).
20. X. Shi, L. Ma, Z. Zhang, Y. Tang, Y. Zhang, J. Han, and Y. Sun, Opt. Commun. **427**, 326 (2018).
21. Y. Wang, C. Sun, H. Li, Q. Gong, and J. Chen, Nanoscale **9**, 11085 (2017).
22. J. Homola, Sens. Actuators B **29**, 401 (1995).
23. Y. Wang, Z. Cao, T. Yu, H. Li, and Q. Shen, Opt. Lett. **33**, 1276 (2008).